Wall-Modeled Large-Eddy Simulation of Turbulent Boundary Layers with Mean-Flow Three-Dimensionality

Minjeong Cho,* Adrián Lozano-Durán,* and Parviz Moin†
Stanford University, Stanford, California 94305
and
George Ilhwan Park‡
University of Pennsylvania, Philadelphia, Pennsylvania 19104

We examine the performance of wall-modeled large-eddy simulation (WMLES) to predict turbulent boundary layers (TBLs) with mean-flow three-dimensionality. The analysis is performed for an ordinary-differential-equation-based equilibrium wall model due to its widespread use and ease of implementation. Two test cases are considered for this purpose: a spatially developing TBL in a square duct with a 30 deg bend, and the flow behind a wall-mounted skewed bump with a three-dimensional separation bubble. In the duct simulation, WMLES is capable of predicting mean-velocity profiles and crossflow angles in the outer region of the flow to within 1–5% error using 10 points per boundary-layer thickness. The largest disagreement (20% error) is observed in the crossflow angles in the bend region, where three-dimensional effects are the most significant. In the skewed bump simulation, it is shown that the present equilibrium wall model with a grid resolution of about 40 points across the three-dimensional separation region predicts mean-velocity profiles and separation location to within 1–3% error. The bubble size and vortex structures in the bump wake are also correctly represented. It is demonstrated that WMLES is capable of achieving accurate results in the separated region and its vicinity, provided that the strong shear layer generated at the apex of the bump is well resolved.

Nomenclature

A_b	=	blockage area
D	=	duct side length
f	=	shedding frequency
H	=	bump height
h	=	channel half-height
L_x	=	computational domain size in streamwise direction
L_y	=	computational domain size in wall-normal direction
L_z	=	computational domain size in spanwise direction
N_{CV}	=	number of control volumes
N_δ	=	number of control volumes across the boundary-layer thickness
$N_{\delta,\text{bend}}$	=	number of control volumes across the boundary-layer thickness within the bend section
Q	=	mean-velocity magnitude
Q_∞	=	freestream value of Q
Re_τ	=	Reynolds number
St	=	Strouhal number
U	=	streamwise mean-velocity component
U_{bulk}	=	bulk velocity
u_τ	=	wall-shear velocity
V	=	wall-normal mean-velocity component
W	=	spanwise mean-velocity component
x	=	streamwise direction
x_s	=	surface of the bump in the streamwise direction
x'	=	streamwise direction in the coordinate system aligned with the local duct centerline
y	=	wall-normal direction
y_s	=	surface of the bump in the wall-normal direction
y'	=	wall-normal direction in the coordinate system aligned with the local duct centerline
z	=	spanwise direction
z_s	=	surface of the bump in the spanwise direction
z'	=	spanwise direction in the coordinate system aligned with the local duct centerline
γ	=	crossflow turning angles
γ_s	=	surface value of γ
γ_∞	=	freestream value of γ
Δs	=	grid resolution of the hexagonal close packed points
θ	=	bump rotation angle
ν	=	kinematic viscosity

*Postdoctoral Fellow, Center for Turbulence Research. Member AIAA.
†Franklin P. and Caroline M. Johnson Professor, Department of Mechanical Engineering, Center for Turbulence Research. Fellow AIAA.
‡Assistant Professor, Department of Mechanical Engineering and Applied Mechanics (Corresponding Author).

I. Introduction

LARGE-EDDY simulation (LES) has become an essential tool for both fundamental studies and real-world engineering applications. However, industrial use of LES has been hampered by its prohibitive grid-point requirements near the wall. This limitation motivates the need for wall models to perform LES at a reduced cost by modeling small-scale near-wall eddies while resolving large-scale eddies in the outer region [1–4]. Although wall-modeled LES (WMLES) has emerged as a viable alternative to the computationally more expensive wall-resolved LES [5], the performance of wall models in nonequilibrium turbulent boundary layers with mean-flow three-dimensionality (3DTBLs) has not yet been carefully assessed. This assessment is particularly important because most widely used wall models to date are built on equilibrium assumptions such as mean-flow two-dimensionality and a statistically steady state.

Skewed mean-velocity profiles and nonequilibrium effects can be caused by the lateral motion of the walls or the spanwise pressure gradient imposed by the bounding geometry, among others. These 3DTBLs exist in a variety of practical problems, such as the bow and stern regions of a ship, sweptback wings, curved ducts, and turbomachinery, to name a few. From the point of view of WMLES, 3DTBLs have peculiar features that are challenging to model. Among these, we can highlight the misalignment of the Reynolds stresses and the mean rate of strain, as well as the counterintuitive depletion of wall friction and Reynolds stress magnitude (e.g., Refs. [6–10]).

Recently, WMLES of a temporally developing 3DTBL in a channel flow with a sudden imposition of spanwise pressure gradient was conducted by Lozano-Durán et al. [11]. The authors considered three wall-model approaches: an ordinary-differential-equation- (ODE)- based equilibrium wall model [12], an integral nonequilibrium wall model [13], and a partial-differential-equation-based nonequilibrium wall model [14]. The performance of the wall models was assessed in the transient channel flow at $Re_\tau = u_\tau h/\nu \approx 1000$, where u_τ is the wall-shear velocity, h is the channel half-height, and ν is the kinematic viscosity. Lozano-Durán et al. [11] quantified the accuracy in predicting the magnitude and direction of the wall stress for increasing complexity of the wall model. Whereas the most comprehensive wall model in terms of incorporating nonequilibrium effects outperformed the simpler approaches, the equilibrium wall model provided the best tradeoff between accuracy when considering ease of model implementation and computational cost.

Recent studies of WMLES in transient three-dimensional (3-D) channel flows also include the works by Carton de Wiart et al. [15], Yang et al. [16], and Bae et al. [17]. Carton de Wiart et al. [15] investigated the performance of WMLES in several cases including acceleration in the streamwise direction, and they showed that WMLES is capable of predicting the wall stress with a good degree of accuracy. Yang et al. [16] also attained accurate results using wall modeling via physics-informed neural networks, whereas Bae et al. [17] employed a novel Reynolds-averaged Navier–Stokes (RANS)-free dynamic wall model to predict the wall stress. In addition to the 3-D channel flow configuration, Cho et al. [18] examined the performance of the ODE-based equilibrium wall model for a spatially developing 3DTBL inside a bent square duct at $Re_\tau = 1200$–2400, following the experiment of Schwarz and Bradshaw [19]. The authors reported a fairly good prediction of velocity and pressure distributions, but with a measurable discrepancy of the crossflow angles in the bend region where the mean three-dimensionality is most pronounced. However, only one WMLES mesh was considered without a grid convergence study.

Another important example of nonequilibrium flows can be found in separated turbulent boundary layers. WMLESs have demonstrated success in predicting trailing-edge separation of hydrofoils and airfoils [14,20,21], as well as airfoils in high-lift configuration [22]. In the recent NASA Juncture Flow Experiment [23], WMLES was successful in recovering the trailing-edge separation bubble to within 10% error using, on average, 10 points per boundary-layer thickness [24], which is remarkable when considering the notably finer resolutions used by RANS-based approaches [23]. Nonetheless, it is unclear whether separated regions should be tackled with WMLES, and the question of whether a wall model is needed in the separated region remains unknown. The recent review by Bose and Park [2] has also pointed out that the use of the no-slip boundary condition might be justified in the separated region since there the flow is governed by slow and large-scale eddies. In that case, it remains to establish how to switch between the no-slip and wall-model boundary conditions.

In this paper, we investigate the performance of WMLES with an ODE-based equilibrium wall model to predict the 3DTBL in a bent square duct and a skewed bump. A preliminary version of the present work can be found in the works of Cho et al. [18,25]. The paper is organized as follows. We first report on the performance of the ODE-based equilibrium wall model in a spatially developing 3DTBL inside a bent square duct, which is accompanied by a mesh convergence study in Sec. II. In Sec. III, we assess the ODE-based equilibrium wall model for LES predictions of 3-D separated flows. A recent experimental study by Ching et al. [26] on flows over a wall-mounted skewed bump with 3-D flow separations is chosen for comparison. Concluding remarks are offered in Sec. IV.

II. WMLES of a Spatially Developing 3DTBL in a Bent Square Duct

A. Computational Details

The flow configuration of the bent square duct is shown in Fig. 1, which follows the experimental setup by Schwarz and Bradshaw [19]. The square duct has a 0.762×0.762 m cross section and a streamwise length of 4.561 m. In the work of Schwarz and Bradshaw [19], the boundary layer became turbulent by a trip wire with a 1.6 mm diameter. A spatially developing 3DTBL was generated by a 30 deg bend that imposes a cross-stream pressure gradient, where the boundary-layer thicknesses are about 3–7% of the duct side length. The surface streamlines were deflected by up to 22 deg relative to the centerline velocity vector. Downstream of the bend, the developed 3DTBL gradually relaxes back to a turbulent boundary layer with two-dimensional mean flow.

We define two coordinate systems following the reference experiment (see Fig. 1). The first coordinate system (x, y, z) is aligned with the upstream section of the bend, where x, y, and z denote the streamwise, wall-normal, and spanwise directions, respectively. The velocity vector in this coordinate system is denoted by (U, V, W). The second coordinate system (x', y', z') is aligned with the local duct centerline.

WMLES is conducted using the code charLES with the Voronoi mesh generator [27]. It solves the compressible LES equations with the constant-coefficient Vreman model as the subgrid-scale (SGS) model [28]. For all simulations, the coefficient of the Vreman model is set to 0.07. The unstructured Voronoi mesh generator, based on a
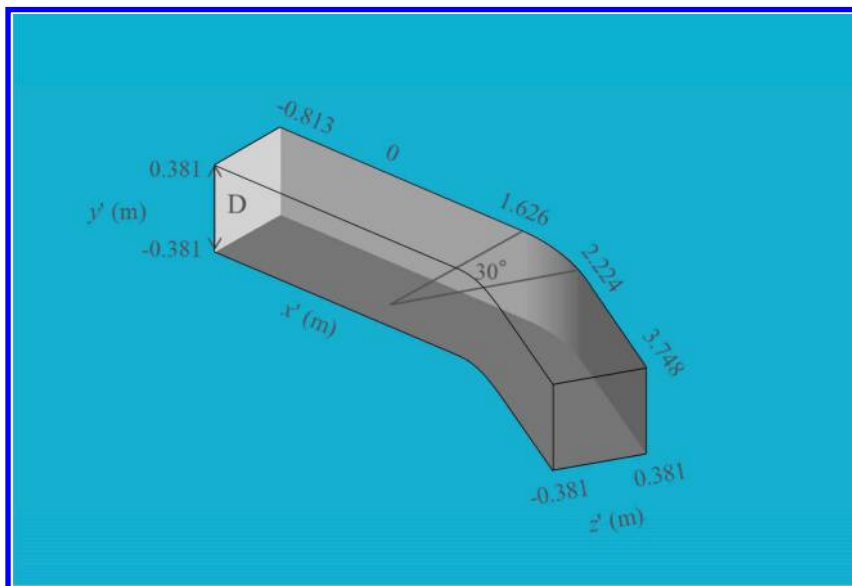

Fig. 1 Flow configuration of the bent square duct. Here, the coordinate system (x', y', z') is aligned with the local duct centerline.

hexagonal close packed (HCP) point-seeding method, is employed to automatically build meshes for arbitrarily complex geometries with minimal user input. Using this platform, high-quality meshes are generated suitable for low-dissipation kinetic energy and entropy-preserving numerical methods for high-fidelity LES [29]. To generate the grid, a surface geometry of the square duct is needed to describe the computational domain, as shown in Fig. 1. Then, the user specifies the coarsest grid resolution of the uniformly seeded HCP points $\Delta s_{\max}$. Clipped Voronoi diagrams are used to generate arbitrary polyhedral cells, where the cell centers are related to these HCP points. To efficiently distribute the points within a volume, sphere packed arrangements are used, which generate uniform cells in regions far from boundaries. Finally, the user can introduce local mesh refinement by specifying volumes (i.e., refinement windows). The length scale discontinuities at the interface of the refinement windows are handled by introducing nested refinement layers between the refinement windows and the coarsest resolution $\Delta s_{\max}$ so that these length scale jumps are never worse than $1:2$. Additionally, Lloyd iterations are used for mesh smoothing, which align the near-wall cells normal to the surface and have a more uniform distance than the original seeding. Therefore, the resulting Voronoi cells are mostly isotropic. For the present WMLES, $\Delta s_{\max}$ is set to 0.01 m and three different mesh refinements are considered, as shown in Table 1 and Fig. 2. The number of Lloyd iterations is 20 in all cases. For case D1, the meshes are refined in the near-wall region so that the number of grid cells across the local boundary-layer thickness N_δ ranges from 8 to 11 along the streamwise direction. The minimum cell size in the wall units is $\Delta s_{\min}^+ = \Delta s_{\min} u_\tau / \nu = 140$, and 30.4 million control volumes are used in total. Case D2 has additional grid refinement, such that the number of control volumes across the boundary-layer thickness within the bend section $N_{\delta,\text{bend}}$ increases from 9 (case D1) to 13–15 (case D2) using 38 million control volumes. In the finest grid resolution (case D3), $\Delta s_{\min}$ is further reduced to 0.00125 m, resulting in $N_{\delta,\text{bend}} = 24$ using 76.4 million control volumes with 16 to 26 points per boundary-layer thickness.

The wall-shear stress from the ODE-based equilibrium wall model [12,20,30] is imposed as the boundary condition at the bottom, top, and side walls. The wall-shear stress from the equilibrium wall model is obtained by integrating

$$\frac{d}{dy}\left[(\mu + \mu_{t,wm})\frac{du_\parallel}{dy}\right] = 0 \quad (1)$$

$$\frac{d}{dy}\left[(\mu + \mu_{t,wm})u_\parallel\frac{du_\parallel}{dy} + c_p\left(\frac{\mu}{Pr} + \frac{\mu_{t,wm}}{Pr_{t,wm}}\right)\frac{dT}{dy}\right] = 0 \quad (2)$$

Table 1 Case setup for the bent square duct

Case	Δs (m)	N_{CV}	N_δ	$N_{\delta,\text{bend}}$
D1	0.0025–0.01	30.4M	8–11	9
D2	0.0025–0.01	38M	8–21	13–15
D3	0.00125–0.01	76.4M	16–26	24
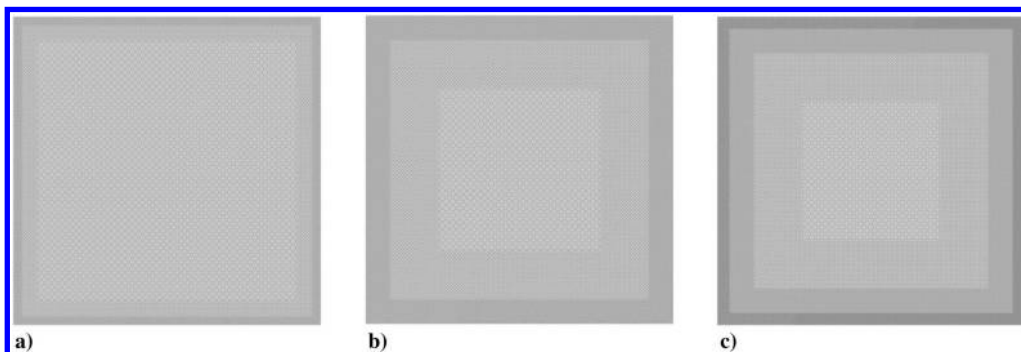
in a layer between $y = 0$ and $y = h_{wm}$, where y is the wall-normal direction, μ is the dynamic viscosity, $\mu_{t,wm}$ is the eddy viscosity, $u_\parallel$ is the wall-parallel velocity, c_p is the specific heat at constant pressure, $Pr = 0.7$ is the Prandtl number, $Pr_{t,wm} = 0.9$ is the turbulent Prandtl number, and T is the temperature. The eddy viscosity is modeled using the mixing length formula

$$\mu_{t,wm} = \kappa\rho y\sqrt{\frac{\tau_w}{\rho}}D \quad (3)$$

$$D = \left[1 - \exp\left(-\frac{y^+}{A^+}\right)\right]^2 \quad (4)$$

where $\kappa = 0.4$ is the von Kármán constant, ρ is the density, τ_w is the wall-shear stress, D is the van Driest damping function, and $A^+ = 17$ is a model coefficient. The walls ($y = 0$) are assumed to be isothermal. The matching location ($y = h_{wm}$) of the equilibrium wall model is at the cell centers of the wall-adjacent control volume. Temporally filtered LES data are provided to the wall model as proposed by Yang et al. [31]. The characteristic-based nonreflective outflow boundary condition is imposed at the outflow plane [32]. For the inflow boundary condition, a synthetic turbulence boundary condition is imposed to provide a realistic turbulent inflow condition that matches the experiment in the upstream section of the bend. Note that the experiment did not report the flow conditions near the trip wire ($x' = 0$ m), and that the boundary-layer measurements are available far downstream of the trip wire ($x' > 0.826$ m). This mandated us to adopt an iterative procedure to adjust a suitable set of inflow parameters to best match the flow condition at the reported stations upstream of the bend. For this purpose, the location of the computational inlet, the mean velocity therein, and the fluctuations superimposed have been tuned. First, a uniform velocity of 26.5 m/s (the freestream value in the experiment) in the streamwise direction is chosen as the mean-velocity field in the inflow plane. Random fluctuations following the standard uniform distribution ($\pm 0.2\%$ the freestream velocity) are then applied to all velocity components. Lastly, the development length (or the location of the computational inlet relative to the bend) is determined by an iterative procedure: a series of preliminary WMLESs of a straight square duct are conducted until the mean-velocity profiles at $x' = 0.978$ in cases D1, D2, and D3 match the reference experiment reasonably well (see Fig. 3). The computational domain so determined starts at $x' = -0.813$. Then, the performance of the WMLES is evaluated at downstream locations. The Reynolds number based on the duct side length ($D = 0.762$ m) and the inlet freestream velocity (26.5 m/s) is 1,400,000. The Reynolds number based on the local momentum thickness and the freestream velocity ranges from 4000 to 9000 ($Re_\tau = 1200$–2400).

B. Results and Discussion

Figure 3 shows the profile of the mean-velocity magnitude ($Q = \sqrt{U^2 + W^2}$) normalized with the local freestream value Q_∞ as a function of the wall-normal distance at various streamwise locations. The velocity profiles from three grids (i.e., cases D1, D2, and D3) are almost on top of each other at each streamwise location, which

Fig. 2 Cross-section grids ($y'-z'$ plane): a) case D1, b) case D2, and c) case D3.
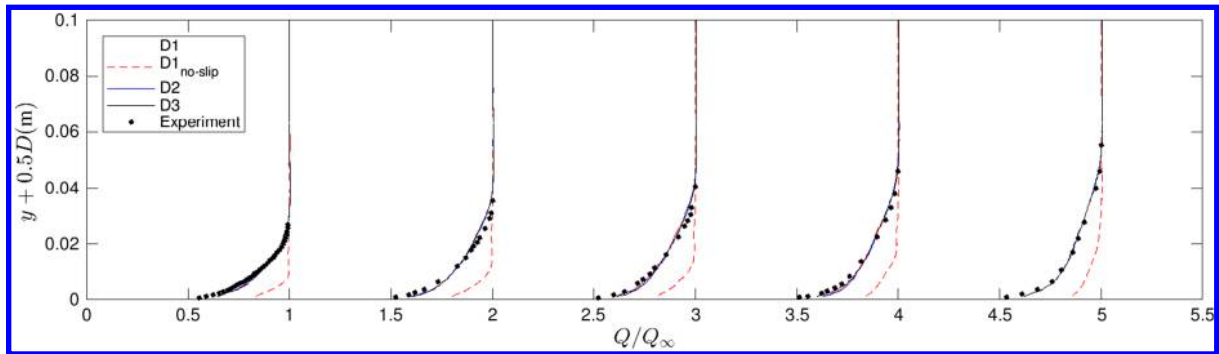
Fig. 3 Mean-velocity profiles at $x' = 0.978$ m (upstream section of bend); $x' = 1.775$ and 2.075 m (inside bend); and $x' = 2.415$ and 2.948 m (downstream section of bend). Here, profiles at $x' = 1.775$, 2.075, 2.415, and 2.948 m are shifted by 1, 2, 3, and 4 on the horizontal axis, respectively. Lines denote present WMLES (cases D1, D2, and D3); circles denote experiment [19]; and dashed lines denote no-slip LES on case D1 mesh (without wall model).

indicates that the WMLES solution has reached grid convergence. For comparison, the results of the no-slip LES (without wall model) using the same coarse mesh for case D1 are also included in the figure.

In the upstream section of the bend at $x' = 0.978$ m, the WMLES solution reproduces the upstream condition of the reference experiment. The mean-velocity magnitude profiles inside the bend (at $x' = 1.775$ m and 2.075 m) and downstream section (at $x' = 2.415$ m and 2.948 m) are also predicted with reasonable accuracy. On the other hand, the discrepancy between the experimental data and the result from no-slip LES is remarkable, indicating the importance of deploying the wall model at the present grid resolutions. In particular, the mean-velocity profiles are overpredicted in the absence of the wall model. This is a common outcome of LES on coarse grids without wall model, in which the lack of support for near-wall Reynolds stresses translates into an excess of streamwise momentum [33].

Figure 4 compares the Reynolds stress profiles from the WMLES to the experiment [19] at various streamwise locations. Here, u', v', and w' indicate velocity fluctuations in streamwise, wall-normal, and spanwise directions, respectively; and $U_{\mathrm{ref}} = 26.5$ m/s. Consistent with the mean-velocity profiles, the Reynolds stress profiles in all cases almost overlap each other at each streamwise location, and they are in reasonable agreement with the experiment. However, the profiles of the no-slip LES (without wall model) using the mesh for case D1 deviate significantly from the experiment.

The local skin-friction distribution along the centerline of the square duct is shown in Fig. 5. The experimental data were reported with 5% uncertainty bands, and the average error between the present WMLES and the experimental data is 8%. Similar to the trends of mean-velocity and Reynolds stress profiles, the skin friction exhibits low sensitivity to different grid resolutions, and the no-slip LES (without wall model) significantly underpredicts the skin friction.

The crossflow turning angles are defined as $\gamma = \tan^{-1}(W/U)$, where W and U are the spanwise and streamwise mean-velocity components with respect to the upstream coordinates (x, y, z). The variations of γ along the axial directions x' are represented in Fig. 6. Hereafter, γ_∞ is γ at the freestream, whereas γ_s is γ at the surface. The results in Fig. 6a show that the angle γ_∞ turns from 0 deg before the bend to 30 deg after the bend, in accordance with the specified geometry. Both WMLES (cases D1, D2, and D3) and no-slip LES (D1 no-slip) predictions are almost on top of each other at the freestream region. The values of γ_∞ from both the WMLES and no-slip LES calculations also show an excellent agreement with the experimental data. This can be ascribed to the essentially inviscid mechanism responsible for the turning of the flow in the core region of the square duct. Assuming an inviscid core region, it can be shown that $\gamma_\infty \approx \theta$, where θ is the geometric turning angle of the duct along the bend. A small discrepancy with experiments (less than 2 deg) is observed in Fig. 6 between the present simulation and the experiment close to the end of the test section ($x' > 3$). In a recent study, Hu et al. [34] conducted WMLES of the same square duct configuration using nonequilibrium wall models and observed a tendency similar to the current WMLES for $x' > 3$. Schwarz and Bradshaw [19] reported
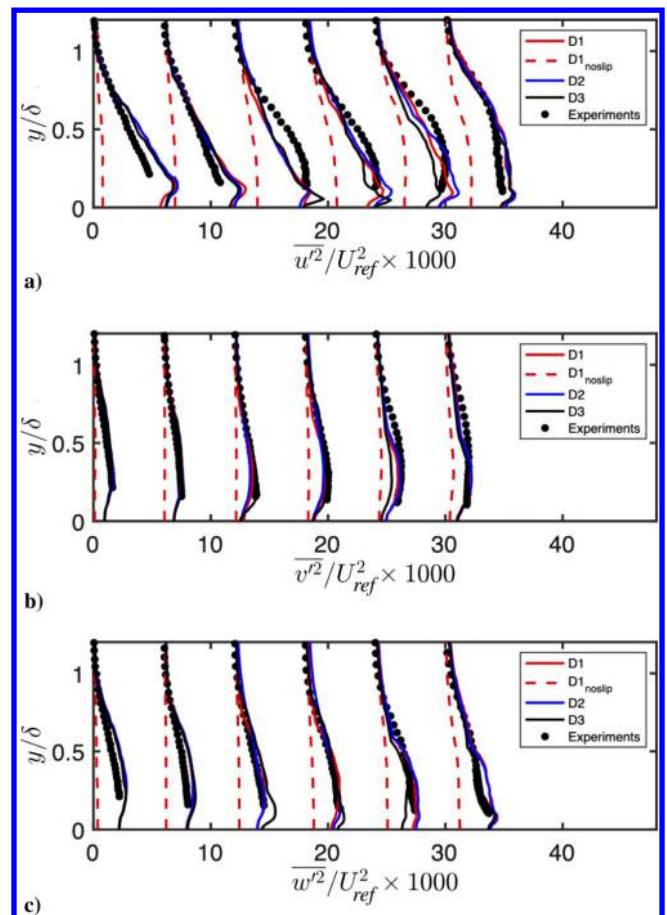
Fig. 4 Reynolds stress profiles at $x' = 0.978$ and 1.435 m (upstream section of bend); $x' = 1.775$ and 2.075 m (inside the bend); and $x' = 2.415$ and 2.948 m (downstream section of bend). Here, profiles at $x' = 1.435$, 1.775, 2.075, 2.415, and 2.948 m are shifted by 6, 12, 18, 24, and 30 on the horizontal axis, respectively: a) $\overline{u'^2}/U_{\mathrm{ref}}^2 \times 1000$, b) $\overline{v'^2}/U_{\mathrm{ref}}^2 \times 1000$, and c) $\overline{w'^2}/U_{\mathrm{ref}}^2 \times 1000$. Lines denote present WMLES (cases D1, D2, and D3); circles denote experiment [19]; and dashed lines denote no-slip LES on case D1 mesh (without wall model).

that the flow direction uncertainty was ± 1 deg, where the mean-velocity field was obtained using a three-hole pressure probe. Therefore, the difference between WMLES and experiments in the downstream of the bend region may be partly due to experimental uncertainties.

Figure 6b shows the streamwise development of $\gamma_s - \gamma_\infty$. The initial increase of the surface crossflow angle upstream of the bend section and its subsequent decrease are qualitatively captured by WMLES for varying grid resolutions (D1, D2, and D3). However,
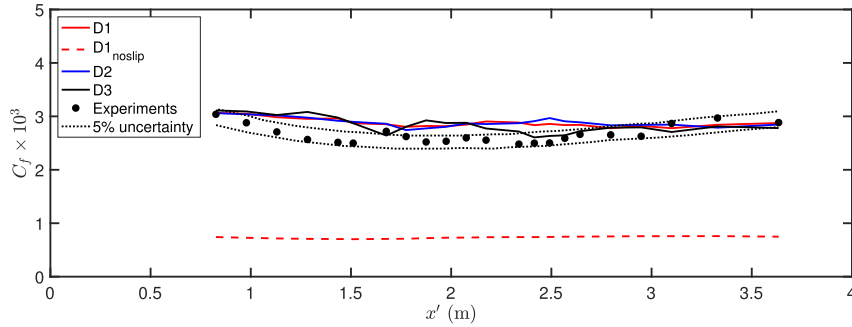
Fig. 5 Local skin-friction distribution along streamwise direction x'. Lines denote present WMLES (cases D1, D2, and D3); circles denote experiment [19]; and dashed lines denote no-slip LES on case D1 mesh (without wall model).
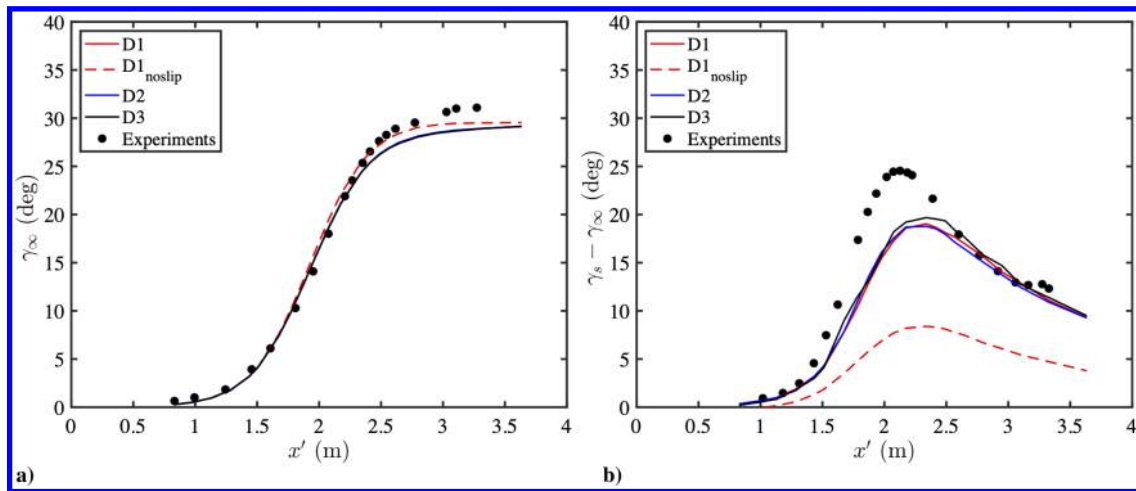

Fig. 6 Crossflow turning angles: a) freestream turning angle γ_∞ distribution along streamwise direction x', and b) surface crossflow angle relative to freestream ($\gamma_s - \gamma_\infty$) along streamwise direction x'. Lines denote present WMLES (cases D1, D2, and D3); circles denote experiment [19]; and dashed lines denote no-slip LES on case D1 mesh (without wall model).

the magnitude of $\gamma_s - \gamma_\infty$ is underpredicted near the bend region by about 20%. These differences between the WMLES and experimental data are mainly localized within the bend, and they decrease as the 3DTBL gradually recovers to the two-dimensional turbulent boundary layer in the downstream section. Refining the WMLES grid resolution (case D3) provides a slight improvement in the bend region compared to coarser grids (cases D1 and D2), but the difference is marginal. The mismatch between WMLES and experiment along the duct bend can be attributed to various causes. The first one is related to the methodology employed to obtain γ_s. Strictly speaking, the angle γ at the wall is $\gamma_s = \lim_{y \to 0} \tan^{-1}(W/U) = \tan^{-1}(\tau_W/\tau_U)$, where τ_W and τ_U are the averaged spanwise and streamwise wall stress, respectively. In the current WMLES, γ_s is obtained from the tangential wall-stress streamlines after the wall stress is averaged in time. Experimentally, the γ_s is measured by oil-flow visualizations at the wall after initial transients of the oil. Albeit both methodologies provide a reasonable description of γ_s, they do not allow for fully consistent one-to-one comparison, which may prompt some disagreement between both results. The second cause for the large errors in $\gamma_s - \gamma_\infty$ is probably more noteworthy, and it arises from the wall-modeling assumptions in Eq. (1). The equilibrium approximation of the current wall model is such that the wall stress vector is aligned with the wall-parallel velocity at the first off-wall location, $\gamma_s = \tan^{-1}(W(x, \Delta_s, z)/U(x, \Delta_s, z))$, which might result in large errors under the presence of acute mean three-dimensionality [11]. It also implies that the mesh refinement alone without the aid of nonequilibrium wall models will not improve the WMLES solution unless the LES grid is able to resolve the three-dimensionality of the mean flow. Hu et al. [34] recently reported that the equilibrium wall model with the minimum wall-normal grid size of 30 in wall units (2.3 times finer than the finest case D3) still showed a discrepancy in predicting the

mean three-dimensionality in the bend region. However, changing the equilibrium wall model to partial-differential-equation (PDE) nonequilibrium wall model was shown to improve the performance of the WMLES.

Figure 7 shows $\gamma - \gamma_\infty$ as a function of the wall-normal direction and complements the picture provided by Fig. 6. The crossflow angle increases until the end of the bend section (Fig. 7a) and decays in the downstream section (Fig. 7b). Figure 7 also shows that the current WMLES predicts the crossflow development and decay, although the angles are smaller than those in the experiment. Consistent with Fig. 6, the discrepancy between WMLES and experiments in $\gamma - \gamma_\infty$ increases with the crossflow development, and it decreases after the bend once the flow starts relaxing to a turbulent boundary layer with two-dimensional mean flow. Figure 7 also shows that no-slip LES significantly underperforms WMLES, but the lack of further improvements with mesh refinements in WMLES hints to the necessity of nonequilibrium wall-modeled accounting for 3-D nonequilibrium effects as discussed earlier in this paper.

A common approach to quantify the 3-D characteristics of the mean-velocity profile is to construct the so-called triangular plot, which comprises the normal U_n and streamwise U_s components of the velocity with respect to the freestream velocity U_e. Here, we use the triangular plot to further evaluate the capability of WMLES to predict mean-flow three-dimensionality. The results, included in Fig. 8, show that current WMLES cases are in reasonable agreement with the experimental data. The freestream flow is represented by $(U_s, U_n) = (1, 0)$. Both WMLES and experiments match for $U_s/U_e > 0.7$, which corresponds to the upper part of the boundary layer. Although not shown, it was also assessed that in this region, WMLES follows the expected inviscid relationship $U_n \approx 2(\gamma - \gamma_\infty)(U_e - U_s)$. The apex of maximum crossflow occurs at $U_n/U_e \approx 0.2$, which is also well
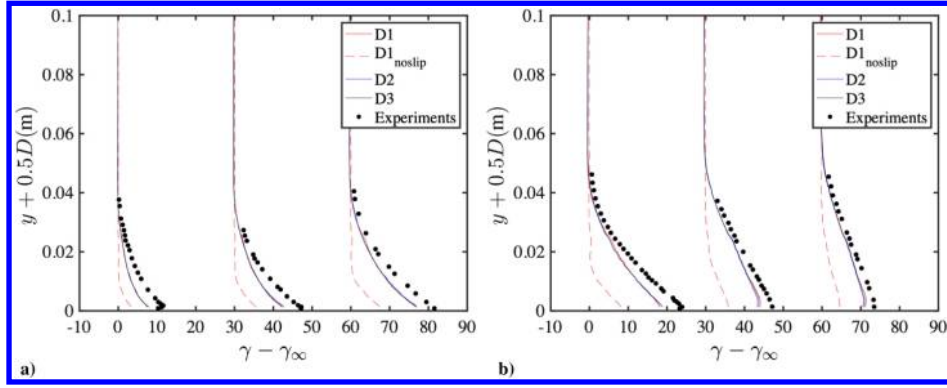
Fig. 7   Crossflow angle relative to freestream: a) crossflow inside bend at $x'(\mathrm{m}) = 1.676, 1.875,$ and 2.075; and b) crossflow in downstream section of bend at $x'(\mathrm{m}) = 2.338, 2.948,$ and 3.329. Here, profiles at $x' = 1.875$ and 2.948 m are shifted by 30 deg and profiles at $x' = 2.075$ and 3.329 m are shifted by 60 deg on the horizontal axis, respectively. Lines denote present WMLES (cases D1, D2, and D3); circles denote experiment [19]; and dashed lines denote no-slip LES on case D1 mesh (without wall model).
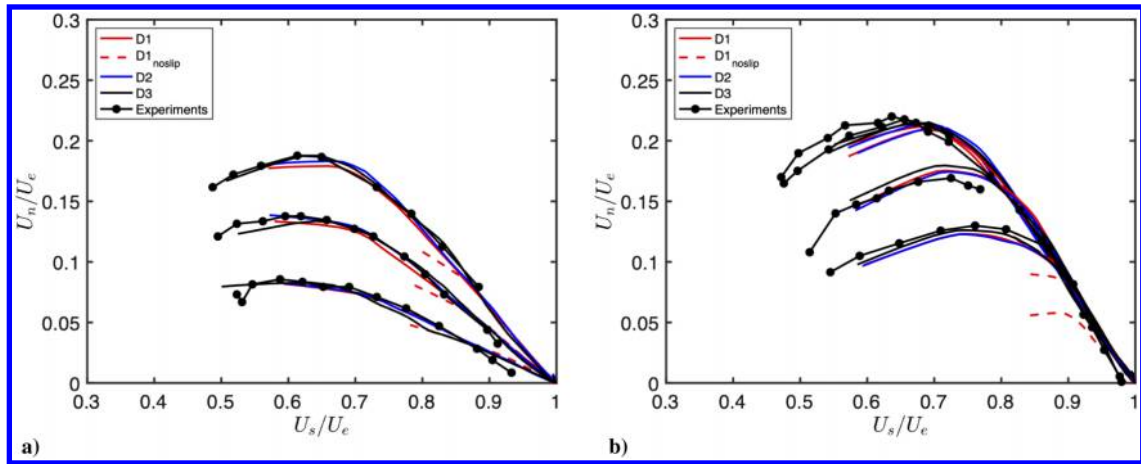
Fig. 8   Triangular plot of velocity: a) crossflow development at $x'(\mathrm{m}) = 1.676, 1.875,$ and 2.075; and b) crossflow decay at $x'(\mathrm{m}) = 2.338, 2.491, 2.948,$ and 3.634. Lines denote present WMLES (cases D1, D2, and D3); circles denote experiment [19]; and dashed lines denote no-slip LES on case D1 mesh (without wall model).

captured by WMLES. The most noticeable difference between WMLES and experiments is the absence of velocities in the range $U_s/U_e < 0.6$ for cases D1 and D2 because these values of U_s are located in the near-wall region of the boundary layer, which is unresolved by their grids. However, the refined grid from D3 is able to correctly predict the experimental values closer to the wall. On the other hand, the no-slip LES case (without wall model) deviates significantly from the experiment: the values attained by U_n are roughly half of those from WMLES and experiments, which points at a lack of three-dimensionality in the mean profile of case $D1_{\mathrm{noslip}}$, consistent with the angles reported in Fig. 7.

III.   WMLES of a Three-Dimensional Flow Separation Behind a Skewed Bump

A.   Computational Details

The computational setup for the three-dimensional skewed bump is illustrated in Fig. 9, which follows the study by Ching et al. [26]. The bump is mounted on the bottom wall of a square duct, and its surface is defined by [26,35,36]

$$y_s = H\left[0.5 + 0.5\cos\left(2\pi\sqrt{\frac{x_s^2}{b^2} + \frac{z_s^2}{a^2}}\right)\right] \tag{5}$$

for $(x_s^2/b^2) + (z_s^2/a^2) < (1/4)$, where x_s, y_s, and z_s denote the surface of the bump in the streamwise, wall-normal, and spanwise directions, respectively; $H(= 19 \text{ mm})$ indicates the bump height, and the parameters a and b are 57 and 42.75 mm, respectively. Here,

the coordinates x_s and z_s are defined with respect to the bump rotation angle θ,

$$x_s = x\cos(\theta) + z\sin(\theta) \tag{6}$$

$$z_s = x\sin(\theta) - z\cos(\theta) \tag{7}$$

The bump angle in the present study is at $\theta = 10$ deg. The origin of the coordinate system is located on the bottom wall below the center of the bump and the Reynolds number based on the bulk velocity (0.83 m/s), and the bump height is 16,000. The Reynolds number based on the wall-shear velocity and the local boundary-layer thickness at $x/H = -4$ is 560. This is a relatively low-Reynolds-number case compared to the bent square duct simulation, where Re_τ ranges from 1200 to 2400.

We compare the WMLES results with those from experimental and LES studies [26,36]. Previous experiments and simulations of the present axisymmetric bump have shown that the flow over the bump separates near the top due to the development of an adverse pressure gradient; i.e., the separation point is not determined by the bump geometry [26,35,36]. A large separation bubble is formed in the wake of the bump, where a common-up vortex pair appears in the mean flow field. Further downstream, this common-up vortex pair evolves into a common-down vortex pair.

We use the same flow solver, charLES, with the Voronoi mesh generator. The boundary conditions for the skewed bump are similar to those of the bent square duct (see Sec. II.A). At the inlet, we prescribed a synthetic turbulence boundary condition, with random fluctuations ($\pm 1.5\%$ the freestream velocity) added to the spatially
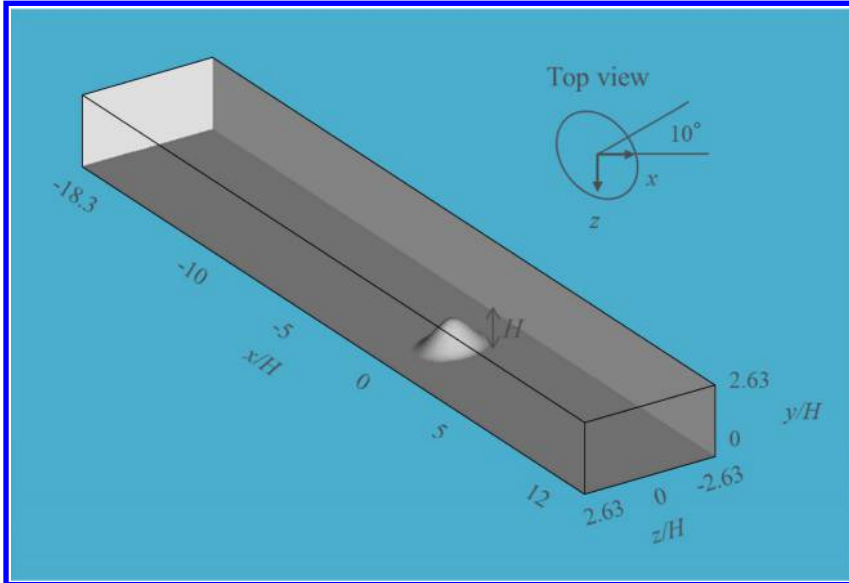
Fig. 9 Flow configuration of the skewed bump. The coordinate origin is located on the bottom wall under the center of the bump.

Table 2   Case setup for the skewed bump

Case	$\Delta s/H$	N_{CV}	$N_{\delta,x/H=-4}$
B1	0.025–0.1	6.7M	20
B2	0.012–0.1	19M	20
B3	0.006–0.1	10.8M	20
B4	0.006–0.1	22.3M	20

uniform freestream velocity of 0.83 m/s. The length of the upstream development section is determined in a separate WMLES of a square duct with the bump removed by matching the mean-velocity profiles at $x/H = -4$ in cases B1–B4 from the reference experiment. Then, we examine the performance of the WMLES at downstream locations. The ODE-based equilibrium wall model from Eqs. (1) and (2) is used to obtain the wall-shear stress at the bottom, top, and side walls, which are also assumed isothermal. The Navier–Stokes characteristic boundary condition is imposed at the outlet [32].

The computational domain size is $L_x \times L_y \times L_z = 575.7$ mm $\times$ 50 mm $\times$ 100 mm. We investigate the grid requirements to capture the correct flow physics of different flow regions by considering a set of four grid resolutions, which are summarized in Table 2 and depicted in Fig. 10. For all the cases, the coarsest grid resolution is set to $0.1H$, and the meshes are refined around the bump and the bottom wall ($-4.5H < x < 5.5H, 0 < y < 1.7H, -2H < z < 2H$; see red-colored region in Fig. 10) such that the grid size in that region is $0.025H$. The boundary-layer thickness at $x/H = -4$ is half the height of the bump ($0.5H$), and the boundary-layer thickness increases in the streamwise direction until it is affected by the adverse pressure gradient as the boundary layer approaches the wall-mounted bump. The present isotropic Voronoi cells result in 20 cells across the boundary-layer thickness at $x/H = -4$. For case B2, an additional refinement window with a grid size equal to $0.012H$ is added to case B1 around the bump and the bottom wall ($-1.5H < x < 3.5H$, $0 < y < 1.2H, -1.8H < z < 1.8H$; see green-colored region in Fig. 10). For case B3, the refinement window with the grid size of
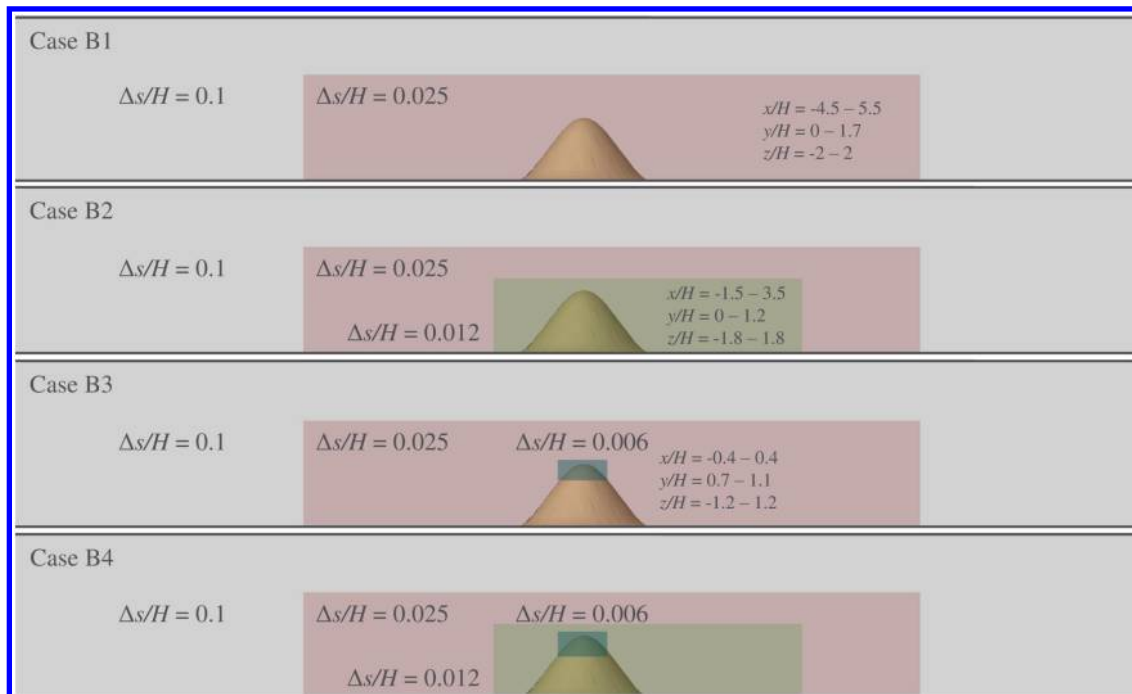

Fig. 10   Schematic diagram of the mesh refinement.

$0.006H$ is added to case B1 on top of the bump ($-0.4H < x < 0.4H, 0.7H < y < 1.1H, -1.2H < z < 1.2H$; see blue-colored region in Fig. 10). Lastly, for case B4, both refinement windows used in cases B2 and B3 are included into case B1 to assess grid convergence. The total number of smoothing iterations is 20 in all cases. It is worth noting that our grids are in the range of ≈ 7–22 million control volumes (Table 2), whereas Ching et al. [26] employed 80 million control volumes to perform the wall-resolved LES of the bump. This outlines the computational savings of WMLES (about four to eight times), despite the moderate Reynolds number of the present case.

B. Results and Discussion

To illustrate the mean-flow configuration across the bump, Fig. 11 shows the mean streamwise velocity contours on the centerplane (i.e., $z/H = 0$) for case B3. The flow separates near the top of the bump ($x/H \approx 0$) and reattaches at $x/H \approx 2$, generating a large separation bubble behind the bump. Figures 12–14 contain the mean streamwise velocity profiles at various streamwise locations for WMLES along with the reference experiment and LES data [26,36]. At the upstream section of the bump (Fig. 12) and the windward side of the bump before the separated region (Fig. 13a), WMLES predicts velocity profiles to within 1% error, regardless of the mesh distribution. The good agreement of the mean velocity with LES data at the upstream section of the bump ($x/H = -4$) also verifies the adequacy of the inlet boundary condition generated by the synthetic turbulence.

Further downstream, the velocity profiles at the leeward side of the bump (Fig. 13b) and at $x/H = 3$ in the downstream section of the bump (Fig. 14) are sensitive to the grid resolution. In case B1, the mean-velocity distributions at the leeward side of the bump (Fig. 13b) and at $x/H = 3$ (Fig. 14) disagree with the reference experiment and LES by up to 20% error. These locations are inside and right behind the main separation bubble, respectively, where WMLES predictions are expected to be the most challenging. Nonetheless, the discrepancy between the WMLES and reference cases is greatly reduced with the additional grid refinements from cases B2–B4, bringing the predictions to within 1% agreement with the reference LES and experiments. Note that case B2 is set to contain the main separation bubble within the green-colored refined region, and case B3 is set to include additional grid cells around the separation point. Overall, the
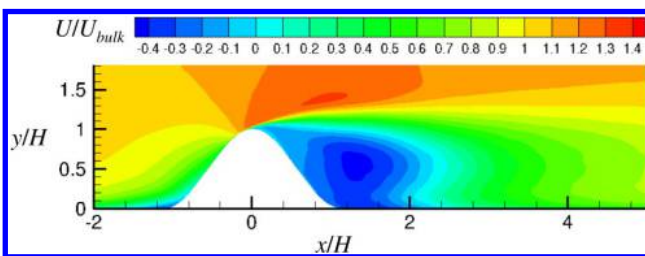
statistics from case B2 and case B3 show remarkable differences, whereas the statistics from case B3 are comparable to case B4 as well as those from the reference studies. Consequently, resolving the thin separated shear layer near the apex (i.e., the blue refinement window in Fig. 10) plays an important role in the successful prediction of the 3-D separated region. This is in agreement with previous WMLES studies in complex geometries [14,21,37,38], which have shown the importance of resolving separated shear layers with proper grid resolution to accurately capture the flow in their vicinity [2]. This observation is also consistent with the analysis from Lozano-Durán and Bae [33], who showed that the errors incurred by WMLES in a given region of the flow scale with the mean shear. Finally, in the far downstream of the separation bubble at $x/H = 5$, the effect of the 3-D separation is weakened and WMLES predicts velocity profiles for all mesh resolutions with reasonably good accuracy.

Fig. 13   Mean-velocity profiles over the bump: a) windward side at $x/H = -1, -0.8$, and -0.4; and b) leeward side at $x/H = 0.4, 0.8$, and 1. Here, profiles at $x/H = -0.8$ and 0.8 are shifted by two and profiles at $x/H = -0.4$ and 1 are shifted by four on the horizontal axis, respectively. Lines denote present WMLES (cases B1, B2, B3, and B4); dashed lines denote no-slip LES on case B3 mesh (without wall model); dashed–dotted lines denote LES [36]; and circles denote experiment [26].

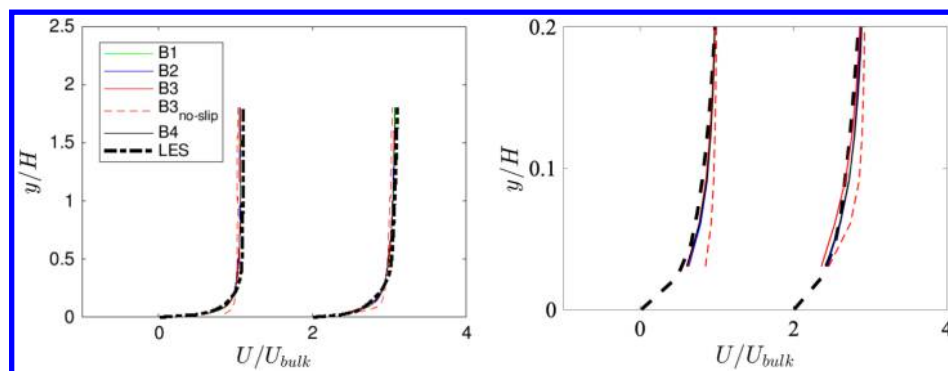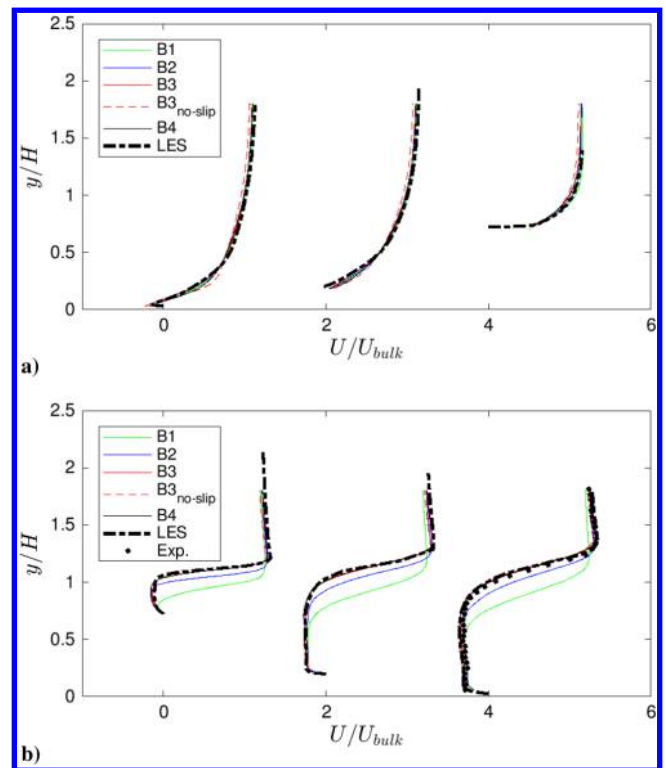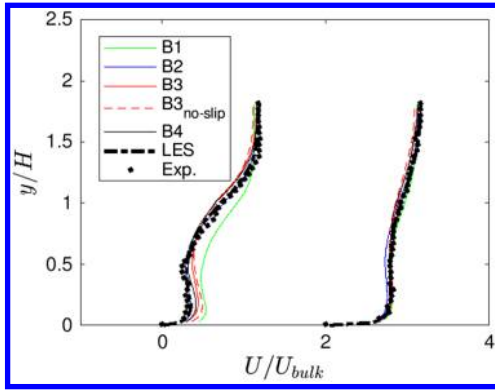**Fig. 11   Contours of mean streamwise velocity at $z/H = 0$ from case B3.**

Fig. 12   Mean-velocity profiles in upstream section of bump at $x/H = -4$ and -2. Here, profile at $x/H = -2$ is shifted by two on the horizontal axis. Lines denote present WMLES (cases B1, B2, B3, and B4); dashed lines denote no-slip LES on case B3 mesh (without wall model); and dashed–dotted lines denote LES [36]. Shown to highlight differences in the near-wall region, profiles up to a) $y/H = 1.7$, and b) $y/H = 0.2$.

Fig. 14 Mean-velocity profiles in downstream section of bump at $x/H = 3$ and 5. Here, the profile at $x/H = 5$ is shifted by two on the horizontal axis. Lines denote present WMLES (cases B1, B2, B3, and B4); dashed lines denote no-slip LES on case B3 mesh (without wall model); dashed–dotted lines denote LES [36]; and circles denote experiment [26].

A better insight into the separation zone is shown in Fig. 15, which portrays a zoomed-in view of the streamwise velocity contours at $z/H = 0$ from cases B1–B4. In the reference LES study [36], the separation point on the centerplane was shown to be located around $x/H = 0$. Here, the separation point is delayed in cases B1 and B2, whereas cases B3 and B4 exhibit a similar separation point to that of Ching and Eaton [36]. The difference between Figs. 15b and 15c highlights again the importance of resolving the shear layer near the apex of the bump, which largely affects the bubble size and reattachment. In addition to the main large separation bubble discussed earlier in this paper, a thin secondary separation bubble was observed at the leeside of the bump by Ching and Eaton [36] in the range

$0.1 < x/H < 0.3$. In WMLES, this secondary bubble is too thin to be accurately captured with the current grid resolution; however, Fig. 15 shows that cases B2–B4 are able to capture an incipient separation zone.

For comparison, the velocity profiles from the no-slip LES (i.e., without the wall model) on the same mesh as case B3 are also included in Figs. 12–14 and denoted by B3$_{\text{no-slip}}$ (red dashed lines). In the upstream section of the bump (Fig. 12), B3$_{\text{no-slip}}$ deviates slightly from WMLES and the experimental results in the near-wall region. However, velocity profiles over the bump (Fig. 13) predicted from the no-slip LES coincide with those from case B3. This indicates that the contribution of the equilibrium wall model in these regions is negligible; hence, the equilibrium wall model naturally deactivates in the separated region at the grid resolution of case B3. We can also argue that further grid refinements would most probably lead to similarly accurate results because the ODE-based equilibrium wall model is consistent with the no-slip condition in the limit of $y^+ \to 0$. Consequently, the use of the equilibrium wall model in the present 3-D separated region does not hinder the performance of WMLES for grid resolutions equal to or below those in case B3. Finally, right after the separation bubble at $x/H = 3$, no-slip LES slightly underperforms the WMLES, but this deviation becomes marginal at $x/H = 5$ in Fig. 14.

Figure 16 compares the Reynolds shear stress $(\overline{u'w'})$ contours at $y/H = 0.5$ from case B3 to the reference LES [36]. Ching and Eaton [36] reported that these contours suggest spanwise movements of the wake because positive streamwise fluctuations are correlated with spanwise fluctuations toward the centerline. The Reynolds shear stress contours predicted from the WMLES show reasonable agreement with the LES, implying that the flow physics in the bump wake region is accurately captured.

Figure 17 illustrates the vortex structures downstream of the bump. As reported in previous studies [26,35,36], a common-up vortex pair
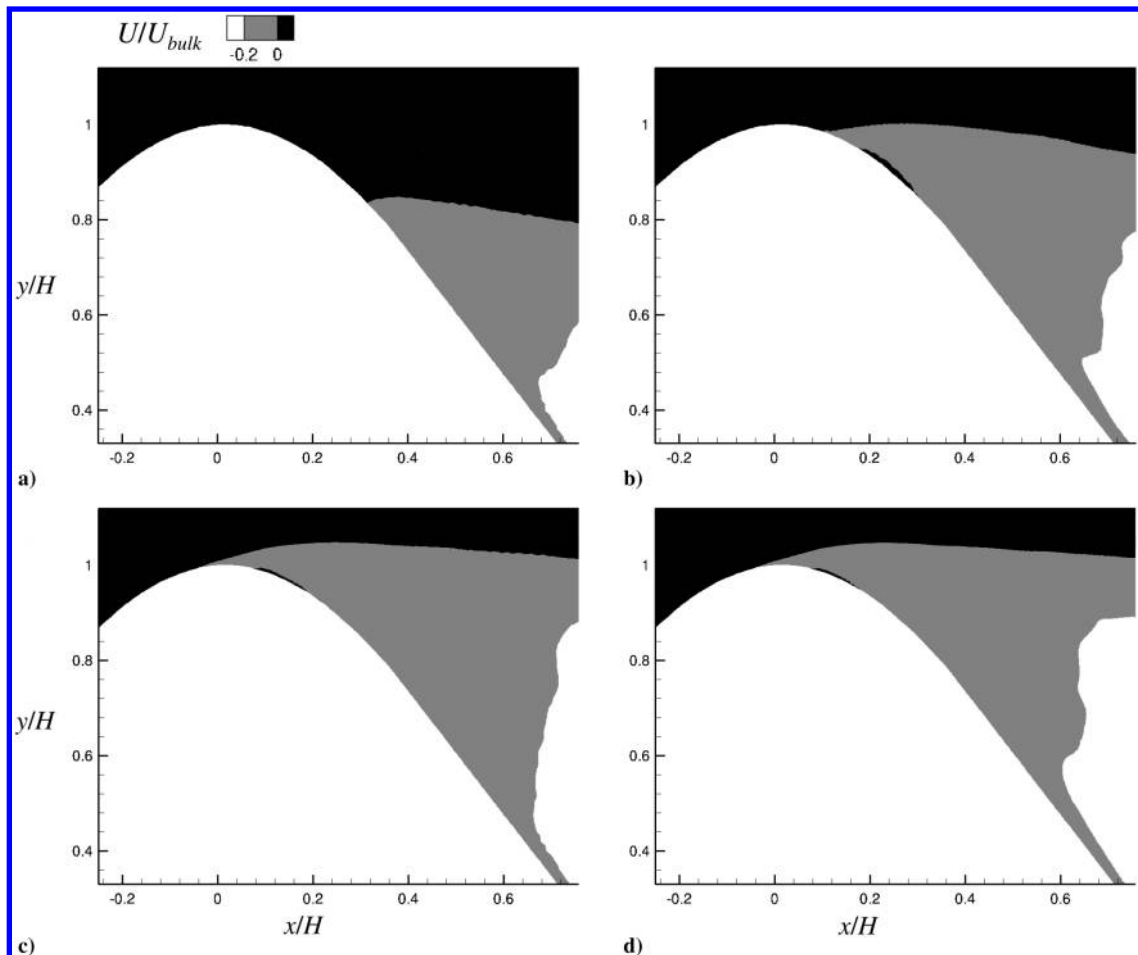
Fig. 15 Contours of mean streamwise velocity at $z/H = 0$ showing separation point and secondary separation bubble: a) case B1, b) case B2, c) case B3, and d) case B4.
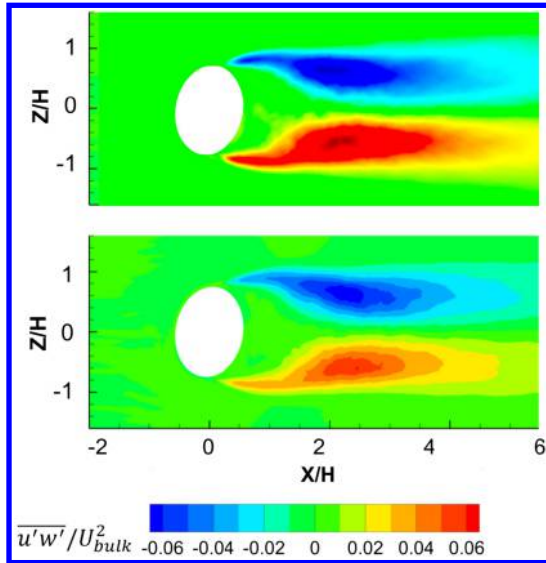
Fig. 16 $\overline{u'w'}/U_{\rm bulk}^2$ contours at $y/H = 0.5$: a) WMLES from case B3, and b) LES [36].
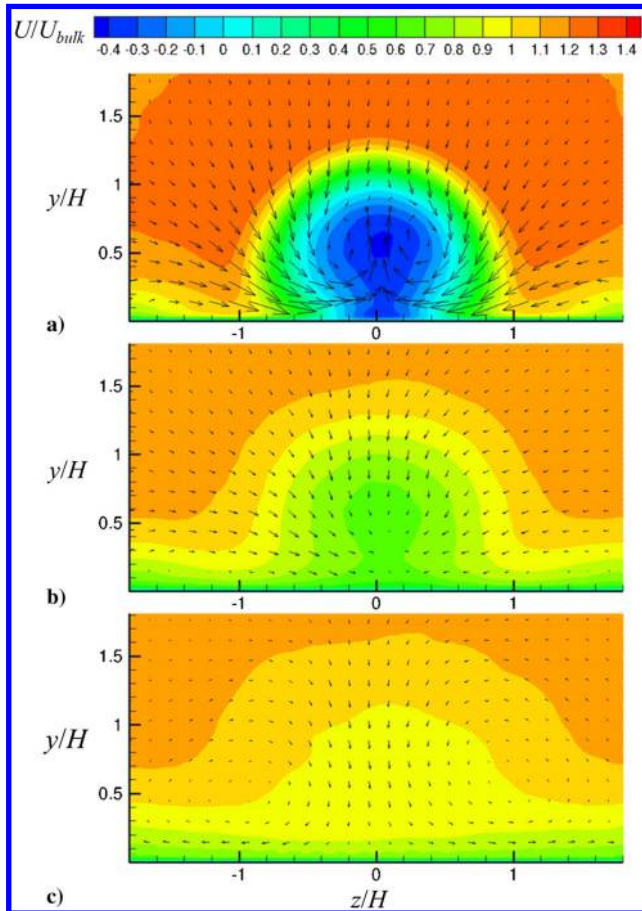

Fig. 17 Mean streamwise velocity contours with in-plane velocity vectors from case B3: a) $x/H = 1.5$, b) $x/H = 4$, and c) $x/H = 8$.

is captured in the separation bubble right behind the bump. This vortex pair evolves into a common-down vortex pair in the far downstream at $x/H = 4.0$. Not only the mean structures but also the shedding frequency behind the bump are captured in the current WMLES, as shown by the velocity power spectra from the probes in the wake region in Fig. 18. Following Ching et al. [26] and Ching and Eaton [36], the Strouhal number is defined as
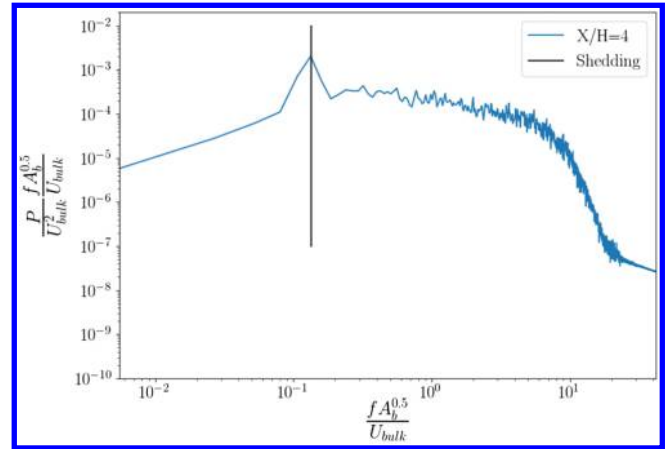

Fig. 18 Velocity power spectra in wake region from case B3. Vertical line denotes Strouhal number from LES [36].

$$St = \frac{f\sqrt{A_b}}{U_{\rm bulk}} \qquad (8)$$

where f is the shedding frequency, A_b is the blockage area, and $U_{\rm bulk}$ is the bulk velocity. The shedding frequency from the WMLES matches the reference LES.

IV. Conclusions

The performance of wall-modeled LES in predicting turbulent boundary layers with mean-flow three-dimensionality was investigated using an ODE-based equilibrium wall model. Two cases were considered: a spatially developing 3DTBL inside a bent square duct [19], and 3-D separated flows in a skewed bump [26,35,36]. In the square duct simulation, WMLES was capable of predicting mean-velocity profiles and crossflow angles in the outer region of the flow to within 1–5% error using 10 points per boundary-layer thickness. However, 20% error was observed in the crossflow angles near the wall in the bend region where the nonequilibrium effects are most significant. This error persisted with increased grid resolution, implying that grid refinement alone without the use of nonequilibrium wall models may not improve the solution in the presence of skewed mean-velocity profiles in the near-wall region. WMLES of the wall-mounted skewed bump showed that the ODE-based equilibrium wall model with a grid resolution of about 40 points across the 3-D separation region predicts the mean-velocity profiles, shedding frequency, and separation location to within 1–3% error. Grid refinement analysis of the bump simulations showed that resolving the incipient flow separation and associated thin shear layer is crucial to attain accurate predictions. Within the separation zone, the current results indicate that WMLES performs well, and reverting to the no-slip boundary condition is not necessary, provided adequate grid resolution is used across the bubble.

Acknowledgment

References

[1] Larsson, J., Kawai, S., Bodart, J., and Bermejo-Moreno, I., "Large Eddy Simulation with Modeled Wall-Stress: Recent Progress and Future Directions," *Mechanical Engineering Revolution*, Vol. 3, No. 1, 2016, Paper 00418.

[2] Bose, S. T., and Park, G. I., "Wall-Modeled Large-Eddy Simulation for Complex Turbulent Flows," *Annual Review of Fluid Mechanics*, Vol. 50, Jan. 2018, pp. 535–561.

[3] Chapman, D. R., "Computational Aerodynamics Development and Outlook," *AIAA Journal*, Vol. 17, No. 12, Dec. 1979, pp. 1293–1313.

[4] Choi, H., and Moin, P., "Grid-Point Requirements for Large Eddy Simulation: Chapman's Estimates Revisited," *Physics of Fluids*, Vol. 24, No. 1, Jan. 2012, Paper 011702.

[5] Slotnick, J., Khodadoust, A., Alonso, J., Darmofal, D., Gropp, W., Lurie, E., and Mavriplis, D., "CFD Vision 2030 Study: A Path to Revolutionary Computational Aerosciences," NASA CR-2014-218178, 2014, pp. 1–51.

[6] Bradshaw, P., and Terrell, M., "The Response of a Turbulent Boundary Layer on an 'Infinite' Swept Wing to the Sudden Removal of Pressure Gradient," National Physical Lab. Rept. 1305, Teddington, Middlesex, U.K., 1969.

[7] Johnston, J. P., "Measurements in a Three-Dimensional Turbulent Boundary Layer Induced by a Swept, Forward-Facing Step," *Journal of Fluid Mechanics*, Vol. 42, No. 4, 1970, pp. 823–844.

[8] van den Berg, B., and Elsenaar, A., "Measurements in a Three-Dimensional Incompressible Turbulent Boundary Layer in an Adverse Pressure Gradient Under Infinite Swept Wing Conditions," National Aerospace Lab. (NLR) TR 72092 U, Amsterdam, 1972.

[9] Elsenaar, A., and Boelsma, S., "Measurements of the Reynolds Stress Tensor in a Three-Dimensional Turbulent Boundary Layer Under Infinite Swept Wing Conditions," National Aerospace Lab. (NLR) TR 74095 U, Amsterdam, 1974.

[10] Bradshaw, P., and Pontikos, N., "Measurements in the Turbulent Boundary Layer on an 'Infinite' Swept Wing," *Journal of Fluid Mechanics*, Vol. 159, April 1985, pp. 105–130.

[11] Lozano-Durán, A., Giometto, M. G., Park, G. I., and Moin, P., "Non-Equilibrium Three-Dimensional Boundary Layers at Moderate Reynolds Numbers," *Journal of Fluid Mechanics*, Vol. 883, Nov. 2020, Paper A20.

[12] Kawai, S., and Larsson, J., "Wall-Modeling in Large Eddy Simulation: Length Scales, Grid Resolution, and Accuracy," *Physics of Fluids*, Vol. 24, No. 1, Dec. 2012, Paper 015015.

[13] Yang, X. I. A., Sadique, J., Mittal, R., and Meneveau, C., "Integral Wall Model for Large Eddy Simulations of Wall-Bounded Turbulent Flows," *Physics of Fluids*, Vol. 27, No. 2, Jan. 2015, Paper 025112.

[14] Park, G. I., and Moin, P., "An Improved Dynamic Non-Equilibrium Wall-Model for Large Eddy Simulation," *Physics of Fluids*, Vol. 26, No. 1, Dec. 2014, Paper 015108.

[15] Carton de Wiart, C., Larsson, J., and Murman, M. S., "Validation of WMLES on a Periodic Channel Flow Featuring Adverse/Favorable Pressure Gradients," *Tenth International Conference on Computational Fluid Dynamics (ICCFD10)*, ICCFD Paper ICCFD10-2018-355, 2018, pp. 1–9.

[16] Yang, Q., Willis, A., and Hwang, Y., "Exact Coherent States of Attached Eddies in Channel Flow," *Journal of Fluid Mechanics*, Vol. 862, Jan. 2019, pp. 1029–1059.

[17] Bae, H. J., Lozano-Durán, A., Bose, S. T., and Moin, P., "Dynamic Slip Wall Model for Large-Eddy Simulation," *Journal of Fluid Mechanics*, Vol. 859, Nov. 2018, pp. 400–432.

[18] Cho, M., Park, G. I., and Moin, P., "Wall-Modeled LES of a Spatially-Developing Non-Equilibrium Turbulent Boundary Layer," *Center for Turbulence Research—Annual Research Briefs*, Stanford Univ., Stanford, CA, 2018, pp. 251–259.

[19] Schwarz, W. R., and Bradshaw, P., "Turbulence Structural Changes for a Three-Dimensional Turbulent Boundary Layer in a 30° Bend," *Journal of Fluid Mechanics*, Vol. 272, April 1994, pp. 183–209.

[20] Wang, M., and Moin, P., "Dynamic Wall Modeling for Large-Eddy Simulation of Complex Turbulent Flows," *Physics of Fluids*, Vol. 14, No. 7, March 2002, pp. 2043–2051.

[21] Bose, S. T., and Moin, P., "A Dynamic Slip Boundary Condition for Wall-Modeled Large-Eddy Simulation," *Physics of Fluids*, Vol. 26, No. 1, Dec. 2014, Paper 015104.

[22] Bodart, J., and Larsson, J., "Wall-Modeled Large Eddy Simulation in Complex Geometries with Application to High-Lift Devices," *Center for Turbulence Research–Annual Research Briefs*, Stanford Univ., Stanford, CA, 2011, pp. 37–48.

[23] Rumsey, C. L., Carlson, J., and Ahmad, N., "FUN3D Juncture Flow Computations Compared with Experimental Data," *AIAA SciTech 2019 Forum*, AIAA Paper 2019-0079, 2019.
https://doi.org/10.2514/6.2019-0079

[24] Lozano-Durán, A., Bose, S. T., and Moin, P., "Prediction of Trailing Edge Separation on the NASA Juncture Flow Using Wall-Modeled LES," *AIAA SciTech 2020 Forum*, AIAA Paper 2020-1776, 2020.
https://doi.org/10.2514/6.2020-1776

[25] Cho, M., Park, G. I., Lozano-Durán, A., and Moin, P., "Wall-Modeled Large-Eddy Simulation of Non-Equilibrium Turbulent Boundary Layers," *Annual Research Briefs, Center for Turbulence Research*, Stanford Univ., Stanford, CA, 2019, pp. 15–28.

[26] Ching, D. S., Elkins, C. J., and Eaton, J. K., "Investigation of Geometric Sensitivity of a Non-Axisymmetric Bump: 3D Mean Velocity Measurements," *Experiments in Fluids*, Vol. 59, No. 143, 2018, pp. 1–14.

[27] Brès, G. A., Bose, S. T., Emory, M., Ham, F. E., Schmidt, O. T., Rigas, G., and Colonius, T., "Large-Eddy Simulations of Co-Annular Turbulent Jet Using a Voronoi-Based Mesh Generation Framework," AIAA Paper 2018-3302, 2018.

[28] Vreman, A., "An Eddy-Viscosity Subgrid-Scale Model for Turbulent Shear Flow: Algebraic Theory and Applications," *Physics of Fluids*, Vol. 16, No. 10, 2004, pp. 3670–3681.

[29] Chandrashekar, P., "Kinetic Energy Preserving and Entropy Stable Finite Volume Schemes for Compressible Euler and Navier-Stokes Equations," *Computer Physics Communications*, Vol. 14, No. 5, June 2013, pp. 1252–1286.

[30] Bodart, J., and Larsson, J., "Sensor-Based Computation of Transitional Flows Using Wall-Modeled Large Eddy Simulation," *Annual Research Briefs, Center for Turbulence Research*, Stanford Univ., Stanford, CA, 2012, pp. 229–240.

[31] Yang, X. I. A., Park, G. I., and Moin, P., "Log-Layer Mismatch and Modeling of the Fluctuating Wall Stress in Wall-Modeled Large-Eddy Simulations," *Physical Review Fluids*, Vol. 2, No. 10, Oct. 2017, Paper 104601.

[32] Poinsot, T., and Lele, S. K., "Boundary Conditions for Direct Simulation of Compressible Viscous Flows," *Journal of Computational Physics*, Vol. 101, No. 1, July 1992, pp. 104–129.

[33] Lozano-Durán, A., and Bae, H. J., "Error Scaling of Large-Eddy Simulation in the Outer Region of Wall-Bounded Turbulence," *Journal of Computational Physics*, Vol. 392, No. 1, Sept. 2019, pp. 532–555.
https://doi.org/10.1016/j.jcp.2019.04.063

[34] Hu, X., Cho, M., and Park, G. I., "Wall-Modeled LES of 3D Turbulent Boundary Layer in a Square Duct with a 30° Bend," *72nd Annual Meeting of the American Physical Society Division of Fluid Dynamics*, Vol. 64, No. 13, 2019, p. 7.

[35] Ching, D. S., Elkins, C. J., Alley, M. T., and Eaton, J. K., "Unsteady Vortex Structures in the Wake of Nonaxisymmetric Bumps Using Spiral MRV," *Experiments in Fluids*, Vol. 59, No. 144, 2018, pp. 1–17.

[36] Ching, D. S., and Eaton, J. K., "Large-Eddy Simulation Study of Unsteady Wake Dynamics and Geometric Sensitivity on a Skewed Bump," *Journal of Fluid Mechanics*, Vol. 885, Dec. 2020, Paper A22.

[37] Kawai, S., and Asada, K., "Wall-Modeled Large-Eddy Simulation of High Reynolds Number Flow Around an Airfoil Near Stall Condition," *Computers and Fluids*, Vol. 85, No. 1, Oct. 2013, pp. 105–113.

[38] Park, G. I., "Wall-Modeled Large-Eddy Simulation of a High Reynolds Number Separating and Reattaching Flow," *AIAA Journal*, Vol. 55, No. 2017, pp. 3709–3721.

P. G. Tucker
Associate Editor